

## James B. Robinson<sup>1</sup>

Electrochemical Innovation Lab,  
Department of Chemical Engineering,  
UCL,  
London WC1E7JE, UK  
e-mail: ucecrobin@ucl.ac.uk

## Donal P. Finegan

Electrochemical Innovation Lab,  
Department of Chemical Engineering,  
UCL,  
London WC1E 7JE, UK;  
National Renewable Energy Laboratory,  
15013 Denver West Parkway,  
Golden, CO 80401  
e-mail: donal.finegan@nrel.gov

## Thomas M. M. Heenan

Electrochemical Innovation Lab,  
Department of Chemical Engineering,  
UCL,  
London WC1E7JE, UK  
e-mail: thomas.heenan.11@ucl.ac.uk

## Katherine Smith

Sharp Laboratories of Europe,  
Oxford Science Park,  
Edmund Halley Road,  
Oxford OX4 4GB, Oxfordshire, UK  
e-mail: katherine.smith@sharp.co.uk

## Emma Kendrick

Sharp Laboratories of Europe,  
Oxford Science Park,  
Edmund Halley Road,  
Oxford OX4 4GB, Oxfordshire, UK;  
Electrochemical Innovation Lab,  
Department of Chemical Engineering,  
UCL,  
London WC1E 7JE, UK;  
Warwick Manufacturing Group,  
University Road, University of Warwick,  
Coventry CV4 7AL, UK  
e-mail: emma.kendrick@ucl.ac.uk

## Daniel J. L. Brett

Electrochemical Innovation Lab,  
Department of Chemical Engineering,  
UCL,  
London WC1E7JE, UK  
e-mail: d.brett@ucl.ac.uk

## Paul R. Shearing<sup>1</sup>

Electrochemical Innovation Lab,  
Department of Chemical Engineering,  
UCL,  
London WC1E7JE, UK  
e-mail: p.shearing@ucl.ac.uk

# Microstructural Analysis of the Effects of Thermal Runaway on Li-Ion and Na-Ion Battery Electrodes

*Thermal runaway is a phenomenon that occurs due to self-sustaining reactions within batteries at elevated temperatures resulting in catastrophic failure. Here, the thermal runaway process is studied for a Li-ion and Na-ion pouch cells of similar energy density (10.5 Wh, 12 Wh, respectively) using accelerating rate calorimetry (ARC). Both cells were constructed with a z-fold configuration, with a standard shutdown separator in the Li-ion and a low-cost polypropylene (PP) separator in the Na-ion. Even with the shutdown separator, it is shown that the self-heating rate and rate of thermal runaway in Na-ion cells is significantly slower than that observed in Li-ion systems. The thermal runaway event initiates at a higher temperature in Na-ion cells. The effect of thermal runaway on the architecture of the cells is examined using X-ray microcomputed tomography, and scanning electron microscopy (SEM) is used to examine the failed electrodes of both cells. Finally, from examination of the respective electrodes, likely due to the carbonate solvent containing electrolyte, it is suggested that thermal runaway in Na-ion batteries (NIBs) occurs via a similar mechanism to that reported for Li-ion cells. [DOI: 10.1115/1.4038518]*

## Introduction

Since their introduction in the early 1990s, Li-ion batteries (LIB) have become ubiquitous in portable energy storage and

have been employed in increasingly compact and power-intensive applications, including automotive power trains [1–3]. While failure rates of Li-ion batteries are estimated to be as low as one in  $40 \times 10^6$ , a number of high-profile incidents [4–7] have resulted in increased concern regarding LIB cell safety [8]. In addition to concerns over the safety of Li-ion cells, the relatively high cost of the cells [9] and potential volatility in Li supply chains [10] have led to increased interest in developing new battery chemistries.

<sup>1</sup>Corresponding author.

Manuscript received July 20, 2017; final manuscript received October 4, 2017; published online December 6, 2017. Assoc. Editor: Matthew Mench.

Despite the now widespread use of Li-ion cells, recent work has seen an increased focus on developing and commercializing alternative battery types for a range of applications. Ni-based cells, such as the NiCd and NiMH, have both been widely used; however, these cells suffer from a low cell potential (1.2 V) in comparison with Li-ion cells (typically around 3.8 V) [11] and also have both a higher internal resistance and lower cycle life than comparable Li-ion systems [12]. Na-based cells have also seen commercialization through the so-called ZEBRA cell, a high-temperature molten salt battery which has a more favorable open-circuit potential of 2.58 V than Ni cells. This battery has been shown to be reliable through extensive in-field testing [13]; however, the high-temperature operation restricts the application of such a cell to stationary or automotive applications. Solid Na metal-based cells, such as the Na-S cell, have also been researched and used in the field although these cells have been found to suffer from dendrite growth under room temperature operation, which has resulted in severe safety concerns [14]. Similar issues have also been reported in Zn-air batteries [15] which have the advantage of higher specific energy densities than Li-ion systems [16], in addition to favorable economic costs [17].

One of the most promising battery types in development is the Na-ion battery (NIB), which uses a Na-based positive electrode which has the benefits of low-cost and global abundance in comparison with the Li compounds used in Li-ion systems [18]. In addition to the economic benefits associated with the charge carrier, the overall cost of the cell can also be reduced by removing the necessity for a copper current collector at the negative electrode as, in contrast to Li, Na does not alloy with aluminum [19]. This configuration also offers potential benefits in terms of safe storage and transport of batteries; once discharged NIB can be stored at zero volts in shorted state, as the aluminum does not dissolve into the electrolyte at low voltages and reprecipitate upon charge [20]. This offers the potential for shipping and storage of cells which contain no energy. Na-ion research has, to date, largely focused on obtaining and optimizing electrode materials with a large number of candidates for both positive and negative electrode materials being investigated. Hard carbon materials which have a reversible capacity of *ca.* 300 mAh g<sup>-1</sup> [21] have typically been used as the negative electrode material due to the low cost of the precursors and ease of production, while this capacity is similar to that of a Li-ion cell (theoretical capacity of 372 mAh g<sup>-1</sup>); hard carbon electrodes suffer from a poor first cycle Faradaic efficiency and capacity fades over multiple cycles [22]. Despite the widespread use of hard carbon, a range of other materials including metal oxides such as Sb<sub>2</sub>O<sub>4</sub> have exhibited reversible capacities approaching 900 mAh g<sup>-1</sup> [23] while the intermetallic compound SnSb/C was shown by Xiao et al. to have a capacity of 435 mAh g<sup>-1</sup> and Faradaic efficiency in excess of 98% after 50 cycles [24].

Positive electrode materials for Na-ion cells have typically focused on structures capable of housing Na<sup>+</sup> ions rather than using metallic Na (as negative electrodes within cells) as these layered oxide materials can avoid dendritic growth at the electrode surface [25,26]. Recent developments in positive electrode materials are summarized by Xiang et al. [27] with theoretical capacities ranging from *ca.* 100–250 mAh g<sup>-1</sup> comparable to LIB. This results in a necessity to have a higher mass loading of the positive electrode in comparison with even a standard hard carbon negative electrode. While Na-ion batteries currently lag behind Li-ion systems in terms of volumetric energy and power density in applications where this is not a large concern, for instance grid scale power storage, this cell may offer a viable alternative in the near future for applications where cost and safety are the key drivers. This can be seen by the recent integration of a Na-ion cell into an e-bike and the significant increase in academic interest in recent times as highlighted by Vignarooban et al. [28]. In conjunction with the research being conducted on improved materials, it is imperative to understand the failure processes which occur in Na-ion cells in order to expedite commercialization opportunities.

Research into the thermal [8,29–31], electrochemical [32–34], and failure mechanisms [35–37] in Li-ion systems are widespread; however, at present similar studies of Na-ion cells are scarce, particularly at the cell level. Recent work performed by Xia and Dahn has examined the safety of positive electrode materials for Na-ion cells showing that NaCrO<sub>2</sub> is a less reactive positive electrode material than LiFePO<sub>4</sub> in similar nonaqueous electrolytes [38]. Here, a combination of accelerating rate calorimetry (ARC) and postmortem materials characterization is used to examine the thermal failure properties of a Na-ion cell compared with a commercially available Li-ion cell. This technique has previously been used to study the failure mechanisms and characteristics of a range of Li-ion chemistries [39–41], examining the effect of temperature on electrolyte degradation and the thermal stability of electrode materials. ARC is a procedure that is used for the measurement of the heat expelled from a material during self-heating. The “heat-wait-search” protocol enables the identification of key thermal steps in the failure of cells, for instance, as described in this work, the onset temperature of thermal runaway in cells. The performance of Na-ion cells is also benchmarked against a similar commercially available LiCoO<sub>2</sub> battery. Pre- and postmortem analysis of the cells is also performed in order to highlight the change in both cell and electrode architectures which in turn may have an influence on the safety of multicell packs.

## Experimental

Accelerating rate calorimetry experiments were performed on two pouch cells of similar energy density and form factor. The Na-ion cell (NIB) used in this work is based on a layered oxide positive electrode material and hard carbon negative electrode material developed by Sharp Laboratories of Europe (90 × 75 × 7 mm, SLE, Oxford, UK), with a polypropylene separator, mixed carbonate solvent (EC:DEC), 1M NaPF<sub>6</sub> salt [42] and a capacity of 12 Wh (3000 mAh). The LIB cell (85 × 45 × 8 mm, AA Portable Power Corp., Richmond, CA) which had a capacity of 10.5 Wh (2500 mAh) is based on a LiCoO<sub>2</sub> (LCO) positive and graphite (negative) electrode material, with a tri-layer (shutdown) separator, and the composition of the electrolyte is EC:DMC with ~1M LiPF<sub>6</sub>. Prior to conducting the ARC experiments, the NIB was fully charged to 4 V (the maximum rated voltage) at 1C, via a constant-current, constant-voltage charging protocol. The LCO cell commercial pouch cell was charged using the same protocol to 4.2 V. The cells were allowed to equilibrate, and the open circuit potential was measured directly prior to the thermal runaway experiment to ensure no capacity fade occurred.

Prior to the failure of each cell X-ray computed tomography (CT), images of both cells in their fresh, fully charged state were

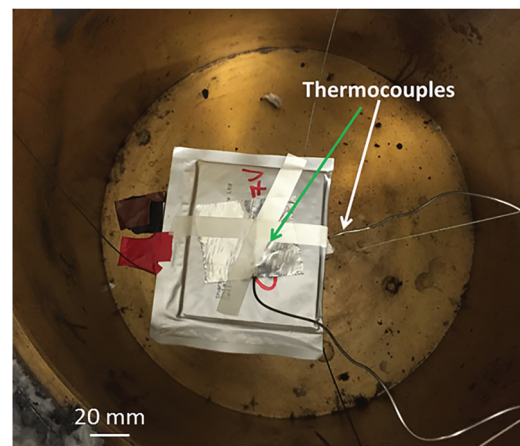


**Fig. 1** NIB cell suspended on wires in the calorimeter, also shown are the location of the thermocouples used for the ARC experiment on the front and rear of the cell

captured using a Nikon XT 225 machine. The geometric configuration of the radiographic scans resulted in a pixel resolution of between 59 and 65  $\mu\text{m}$ . In all cases, an accelerating voltage of 210 kV with a tungsten target was used to generate 3176 projections of the cells. The radiographic dataset acquired was reconstructed using a filtered back projection algorithm built into the commercially available CT PRO 3D software with subsequent visualization achieved using AVIZO FIRE 9.2 (FEI Company, Hillsboro, OR).

Accelerating rate calorimetry was performed inside a calorimeter (Phitec Battery Test Calorimeter, HEL Group, Hertfordshire, UK) using the heat-wait-search method. This is a standard method that involves heating the sample to the start temperature, following which a period is observed for the environmental temperature to stabilize followed by the measurement of any self-heating. For both cells, self-heating rates in excess of  $0.02\text{ }^\circ\text{C min}^{-1}$  were tracked until the heating stopped. Once the self-heating had finished, the set temperature was raised by  $5\text{ }^\circ\text{C}$  and the process repeated until thermal runaway occurred: in order to ensure safe operation, a maximum temperature of  $280\text{ }^\circ\text{C}$  was set in both instances. Temperature change was monitored using two K-type thermocouple which were placed in similar locations on opposing sides of the cell, as shown in Fig. 1. The cell was then suspended in the center of the calorimeter (see Fig. 1) to ensure radiative effects were accounted for. After thermal runaway, the calorimeter was left to cool to ambient temperature before postmortem X-ray CT of the failed cells was performed using the Nikon XT 225 instrument. In all cases, an accelerating voltage of 200 kV was used with the power subsequently optimized to provide sufficient counts of 60,000 on the detector.

Pre- and postmortem scanning electron microscope (SEM) images were obtained using a Zeiss EVO 10 SEM (Carl Zeiss AG, Germany) with imaging being performed at 10 kV using the secondary electron (SE1) signal to obtain images of the NIB cell and at 15 kV using the same SE1 signal to obtain images of the Li-ion cells before and after failure. Magnifications of approximately  $10,000\times$  were obtained resulting in a pixel size of 29 nm in all cases. The fresh samples were prepared in a glovebox before later being transferred, in a sealed container, to the SEM minimizing air and moisture exposure.

## Results and Discussion

Accelerating rate calorimetry was performed in order to induce thermal runaway in both NIB and LCO cells. The temperature profiles obtained for both types of cell are shown in Fig. 2. The initial plateaus observed for NIB and LCO cells before the initial exothermic event are thought to be the initial breakdown of the solid electrolyte interphase (SEI). It is observed that the time

before the first exotherm is significantly longer in the LCO cell compared to the NIB. In both cases, an initial exotherm is seen to initiate between  $30$  and  $50\text{ }^\circ\text{C}$ ; this initial temperature rise has previously been suggested to be as a result of the breakdown and subsequent reformation of the SEI layer in Li-ion batteries [43]. The higher temperature exotherm for LCO cells compared to NIB and the longer time taken to reach this first exothermic event are likely due to the stability of the SEI layer; with the SEI in Li-ion batteries being more stable to higher temperatures. Sodium salts are in general more stable than lithium salts, and therefore it is not unreasonable to assume that the SEI in NIB is significantly more soluble than LIB. The earlier onset temperature and shorter time to reach this first exothermic event in NIB suggests that it is important to consider the SEI formation further. To our knowledge, formation studies have not yet been performed for NIB, nor electrolyte additives investigated, and this result highlights the need for more detailed studies to stabilize and understand NIB SEI further. Once this initial exotherm has concluded, a second exotherm is visible which indicates the onset of thermal runaway. This is seen in the profiles shown in Fig. 2 with thermal runaway apparent due to a sudden increase in the temperature of the cell with the region highlighted. A difference between the cells is seen with a second plateau region visible in the temperature trace of the LCO cell; this may be attributed to the presence of a so-called “shutdown separator” in the LCO cell which is not incorporated in the NIB cell. These shutdown separators are composite structures consisting of a tri-layer of polypropylene (PP), polyethylene (PE), and polypropylene (PPIPE/PP) designed to delay or indeed prevent thermal runaway in the case of electrical abuse [44,45]. It is also possible that within this temperature window, the LCO cell ruptured, resulting in the Joule–Thompson effect occurring—an effect which has previously been observed in 18,650 type Li-ion cells [36]. Despite the integration of safety devices such as the shutdown separator, thermal runaway will only be delayed during ARC due to the temperature increasing until failure.

To evaluate the respective thermal runaway process, the self-heating rate of both cells during the ARC experiment was calculated; these results are outlined in Fig. 3 with a clear discontinuity in the LCO cell visible, once again most likely due to the rupture of the LCO cell. It is shown in Fig. 3 that the self-heating rate for the NIB cell is significantly lower at the initial stages of the experiment (corresponding to the blue line). In this region, thermal runaway has not yet occurred in either cell. As the energy density is similar between both cells, this suggests the initial degradation and decomposition of the components of LCO cells associated with elevated temperatures are mildly less exothermic than those observed in NIB systems; however, the thermal runaway event is significantly more exothermic in the LCO cell than the NIB battery.

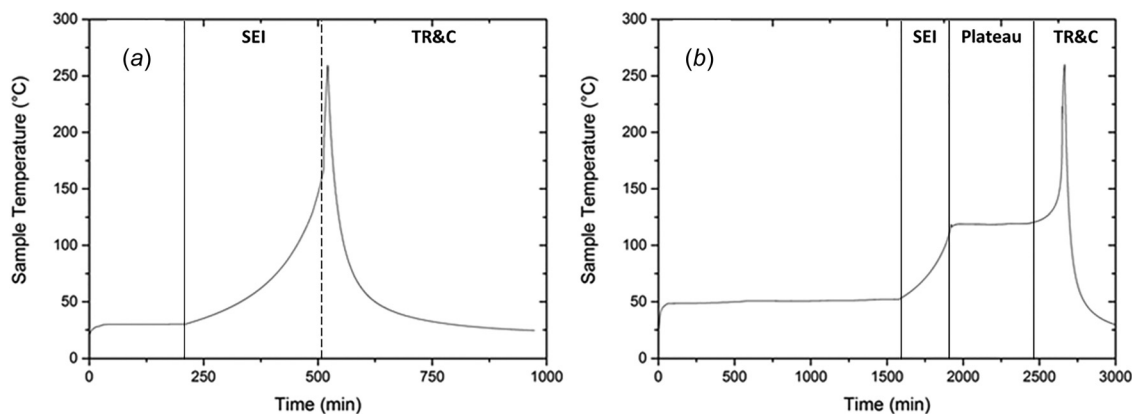
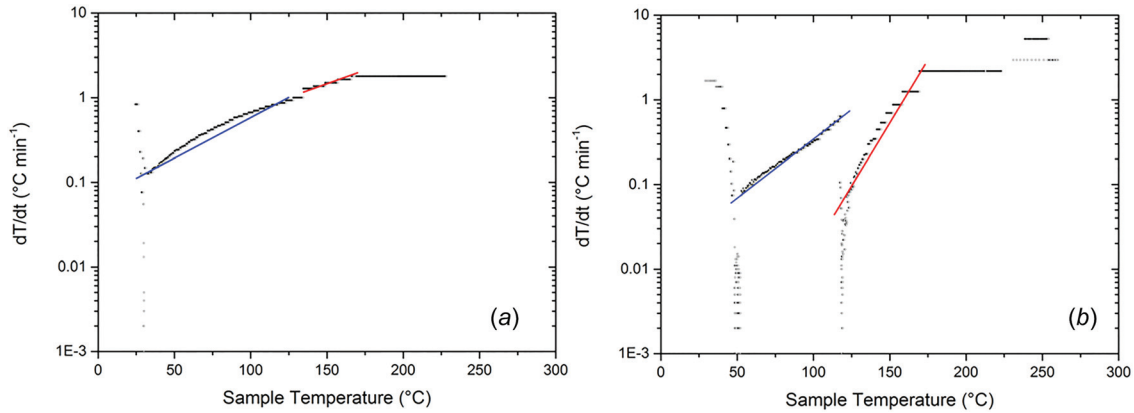


Fig. 2 SEM images of (a) pristine, and (b) failed, negative electrodes from the LCO cell, (c) pristine  $\text{LiCoO}_2$  positive electrode, (d)  $\text{LiCoO}_2$  positive electrode after thermal runaway has occurred. All images are obtained using the SE1 signal at 15 kV accelerating voltage with magnifications of approximately 10,000 yielding a pixel size of 29 nm in all cases.



**Fig. 3** SEM images of (a) pristine, and (b) failed, negative electrodes from the LCO cell, (c) pristine  $\text{LiCoO}_2$  positive electrode, (d)  $\text{LiCoO}_2$  positive electrode after thermal runaway has occurred. All images are obtained using the SE1 signal at 15 kV accelerating voltage with magnifications of approximately 10,000 yielding a pixel size of 29 nm in all cases.

**Table 1** Rate of reactions of the isotherms observed in Fig. 3 corresponding to the initial degradation of the cell (blue, as seen in Fig. 3) and thermal runaway (red, as seen in Fig. 3)

Reaction rate ( $\text{min}^{-1}$ )	Initial degradation (blue)	Thermal runaway (red)
NIB	$9.92 \times 10^{-3}$	$5.68 \times 10^{-2}$
LCO	$7.65 \times 10^{-3}$	$2.13 \times 10^{-1}$

The rate of change of temperature after the onset of thermal runaway occurs within the cells also shows a stark difference. The discontinuity provided by the shutdown separator prior to thermal runaway is once again visible for the LCO cell in Fig. 3(b) with the self-heating rates occurring during the initial stages of thermal runaway also highlighted with a red line. Due to the rapid nature of thermal runaway and the upper safety limit imposed on the ARC experiment, it was not possible to capture the self-heating rate to the conclusion of the cell failure. Despite this, it is evident from Fig. 3 that the thermal runaway reaction is significantly faster over the temperature range in a LCO cell; with the larger

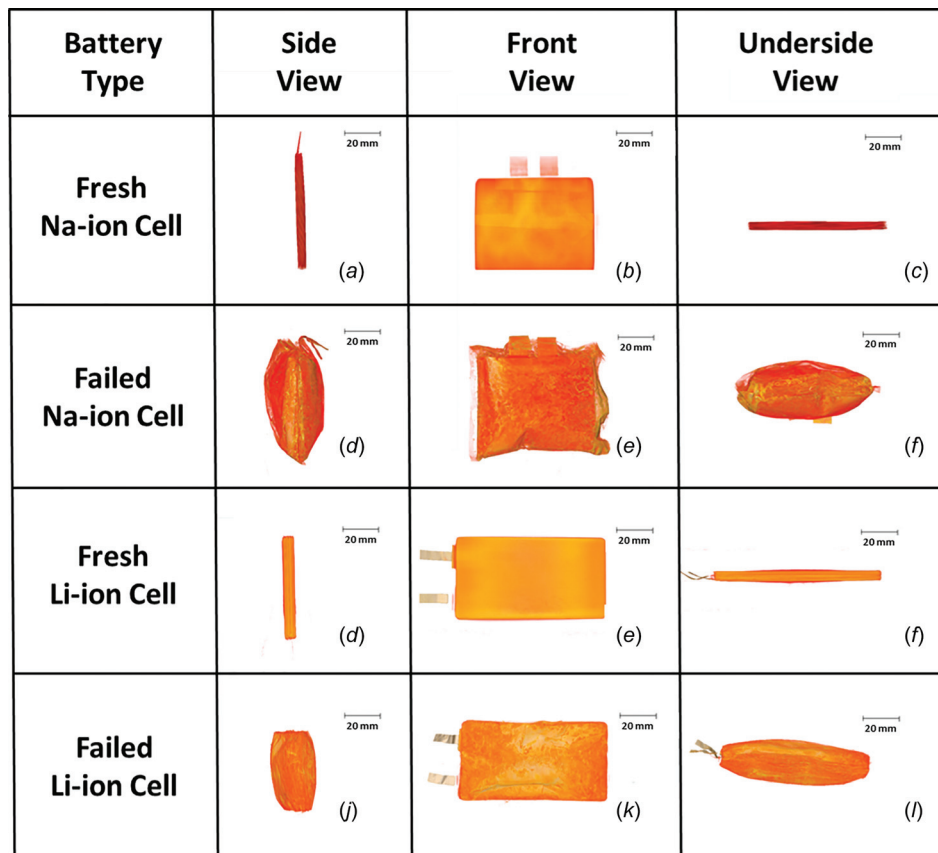


**Fig. 4** Cell scale tomographic renderings of the charged ((a)–(c)) and failed ((d)–(f)) NIB cell and the charged ((g)–(i)) and failed ((j)–(l)) LCO cell showing the extent of deformation associated with thermal runaway

gradient visible in the self-heating rate of the LCO cell indicative of a higher reaction rate as shown in Table 1.

This increased reaction rate reduces the time frame for the heat to dissipate and consequently would result in a faster temperature rise when incorporated into a pack or module. In turn, this suggests that NIB cells fail with less risk of cell-to-cell propagation of thermal runaway and therefore may be a safer option in situations where concerns over thermal runaway exceed the requirement for the comparably higher volumetric/gravimetric power densities provided by Li-ion cells. It must also be noted that the LCO cells used in these experiments are not considered the most unstable [31] and cells with cathodic materials such as nickel manganese cobalt or nickel cobalt aluminum oxide, which are widely used in electric vehicles and will exhibit even greater rates of heat generation during thermal runaway as a result of the more exothermic decompositions of the respective positive electrodes.

X-ray CT was performed on the charged NIB and LCO cells both before and after ARC: this nondestructive technique enables the full visualization of the architectural changes that occur within the cells due to the thermal runaway event. Full three-dimensional renderings of the respective cells are shown both prior to and after the failure of batteries in Fig. 4. The current collecting tabs are located on different edges of the respective cells and the orthogonal planes are in view for comparison, i.e., the front view is the ( $x, y$ ) plane, and the side view ( $x, z$ ) and the underside view are the ( $y, z$ ) plane. These images show the significant alterations in both the internal and external structures as a result of the thermal runaway.

It is clear from Fig. 4 that thermal runaway has a catastrophic effect on the external housing of both cells. Ruptures are visible at the current collecting tabs for both batteries (Figs. 4(d) and 4(f)) while an additional rupture is also seen to occur in the side of the NIB cell (Fig. 4(e)). These differences may be due to a variation of the quality of the seal achieved in each cell with the commercial LCO cell being subjected to a more rigorous quality control procedure than the NIB cell which was produced in a small batch. In order to quantify the extent of the deformation caused by thermal runaway, dimensional measurements were taken along the major orthogonal axes of the individual cells before and after failure as outlined in Table 2.

It is clear from Table 2 that the NIB cell suffers more severe distortion than the LCO cell during thermal runaway. This may be due to a variation in the sealing strategy of the cells; however, in this instance, it is important to stress that while a single cell which experiences such expansion changes may be acceptable, should multiple cells be combined together in a pack this could lead to heightened stress on the module. In all cases, it is seen that some changes to the cell structure occur; however, for both the LCO and NIB cells, the largest of these deviations occur due to gases passing through the cell toward the seal along which the current collecting tabs protrude. While this is useful in order to remove potentially toxic gases from the module, it may be useful to employ a small pressure relief component in the cells to mitigate against the large architectural distortions in cells and reduce the mechanical stress on components within a battery pack, such as is typically observed in spiral wound cell geometries. It should be

**Table 2** Extent of deformation as a percentage of original volume observed in NIB and LCO pouch cells as a result of thermal runaway. The orientations described below show (a) the side view in Fig. 4, (b) the front view in Fig. 4 and (c) the underside view in Fig. 3 in all cases along the vertical axis. Note the measurements did not include the current collecting tabs as these positions were altered when the cells were placed in the calorimeter.

Expansion (%)	(a)	(b)	(c)
NMM	20.76	-12.69	659.29
LCO	3.85	2.51	399.45

noted that the NIB cells used in this work were produced in small batches; as such, further optimization of the electrolyte may result in reduced gas generation further improving the safety of the cells.

The extent of damage to the internal macrostructure is most clearly seen by taking orthogonal slices through the reconstructed data set. These ortho-slices are shown in Fig. 5 as a side view highlighting how the electrode layers are separated as a result of the thermal runaway.

The separation of the electrode layers due to thermal runaway is clearly visible for both the NIB (a, b) and LCO (c, d) cells shown in Fig. 5. The effect of the structural deformations which occur in the cell on the thermal runaway event cannot be quantified here; it is, however, highly likely that during the failure the positive and negative electrodes came into contact with each other resulting in internal short circuiting and additional heating. Fractures in the current collecting layers can also be seen in both cells suggesting a large pressure relief event which cause the layers to

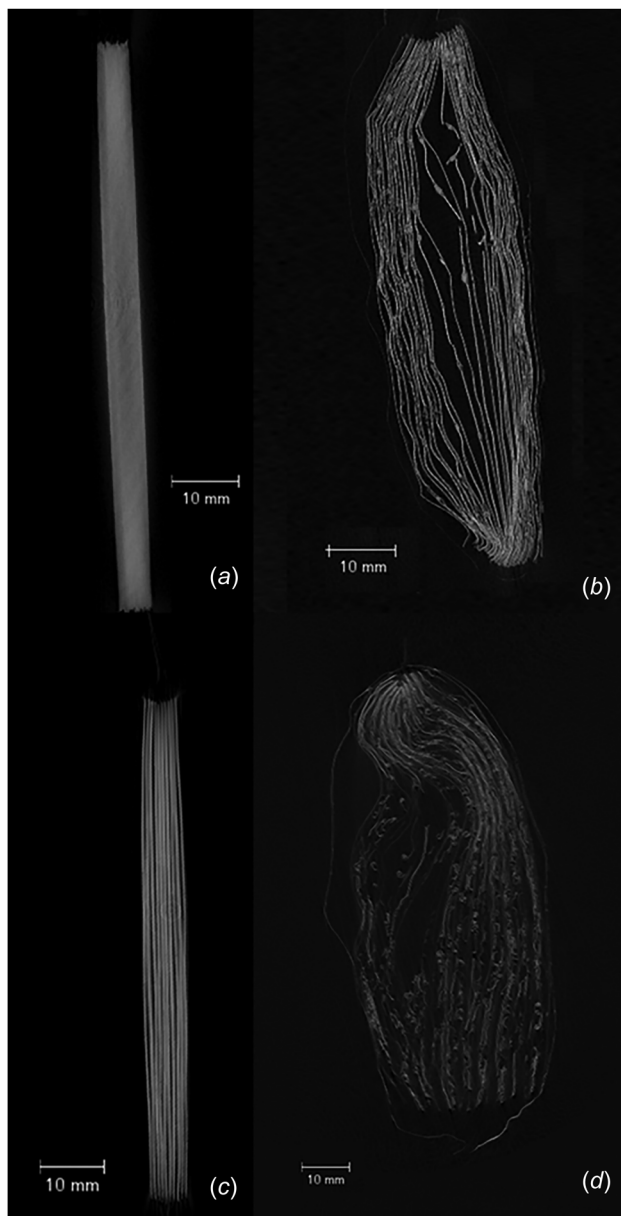


**Fig. 5** Orthogonal slices showing the internal arrangement of electrode layers for charged NIB (a) and LCO (c) cells and the extent of deformation caused by thermal runaway for the same NIB (b) and LCO (d) cells

fracture, similar to effects previously reported by Finegan et al. [35]. Additionally, the electrode stack is seen to rise from the base of the pack in the NIB cell which contributes to the larger expansion in this plane, noted in Table 2.

Once the radiographic scans were completed both the NIB and LCO cells were removed and visually inspected. Charring visible on the surface of the pouch was observed in both instances; however, it was seen to be more pronounced on the NIB cell as seen in Fig. 6.

Deconstruction of the failed cells was performed in order to prepare samples for subsequent SEM imaging. During this process, it was noted that the NIB cell's aluminum current collector, upon which the positive electrode material was printed, remained largely intact; with only small perforations observed, likely due to the release of gas upon the rupture of the cell. This indicates that the maximum internal temperature of the cell did not reach 660 °C, the melting point of aluminum, throughout the thermal runaway process. This is in stark contrast to work which has previously shown that nickel manganese cobalt oxide type Li-ion cells (although in a different format) can exceed internal temperatures of a least 1085 °C during thermal runaway [35,36]. It was also seen in the failed NIB cell that the adhesion of the failed positive electrode material was weak as a result of the gas generation at this portion of the cell. While the hard carbon negative electrode remained largely intact and attached to the aluminum current collecting layer, this electrode was observed to be highly brittle in nature, in comparison with a fresh electrode, as a result of the failure of the cell.

In contrast to the failed NIB cell, the aluminum positive electrode current collecting layer of the LCO cell was seen to have largely disintegrated due to the thermal runaway process. In both cells, however, the negative electrode current collecting layers remained undamaged. The copper current collector used in the LCO cell was seen to have remained wholly intact, suggesting the maximum internal temperature reached during thermal runaway was in the region of 660–1085 °C. It was observed that the positive electrode material layer was significantly more brittle after

failure than a fresh sample obtained from an identical cell; and, as with the NIB cell, the adhesion of the positive electrode was reduced when compared to a pristine sample (Fig. 6).

Microstructural examinations of both the NIB and LCO cells were conducted using SEM. In order to evaluate the condition of the failed cells, pristine samples were also obtained from identical cells in a glove box and transferred via air-sealed containers to the SEM.

Figure 7 shows the SEM images obtained of pristine and failed negative electrode (*a, c*) and positive electrode (*b, d*) of the NIB cell. It is evident that the negative electrode of the cell, which is composed of a hard carbon, remains intact as a result of thermal runaway. This is to be expected as the hard carbon used in electrodes is formed via pyrolysis reactions typically performed at temperatures in excess of 1000 °C [46]. In contrast, the microstructure of the positive electrode is observed to alter as a result of the failure. Portions of the positive electrode were observed to be fully removed from the Al current collector (likely as a result of gas generation) alongside generally reduced adhesion of the electrode layer to the current collector: this reduced adhesion is also visible in the ortho-slices shown in Fig. 5 with a delamination of the electrode from the remaining current collector observed.

Figure 8 shows similar SEM images obtained for the LiCoO<sub>2</sub> cell showing both the anode and cathode before (*a, c*) and after (*b, d*) thermal runaway. In contrast to the Na mixed metal (NMM) cell, changes in the microstructure are evident for both electrodes in the LCO cell. The graphitic anode (*a, b*) is seen to significantly reduce in particle size. Visible porosity is also observed throughout the failed anode in Fig. 8(*b*), which suggests a proportion of the graphite may have oxidized to form CO<sub>2</sub> as has previously been reported [47]. The rate of this process has been noted to be increased by the presence of transition metals [48] which may suggest crossover of metallic elements from cathode to anode following the melting of the separator. In contrast to the NMM system, the particle morphology of the cathode does not change drastically as a result of thermal runaway. However, it is evident that the cathode also shows increased porosity after thermal

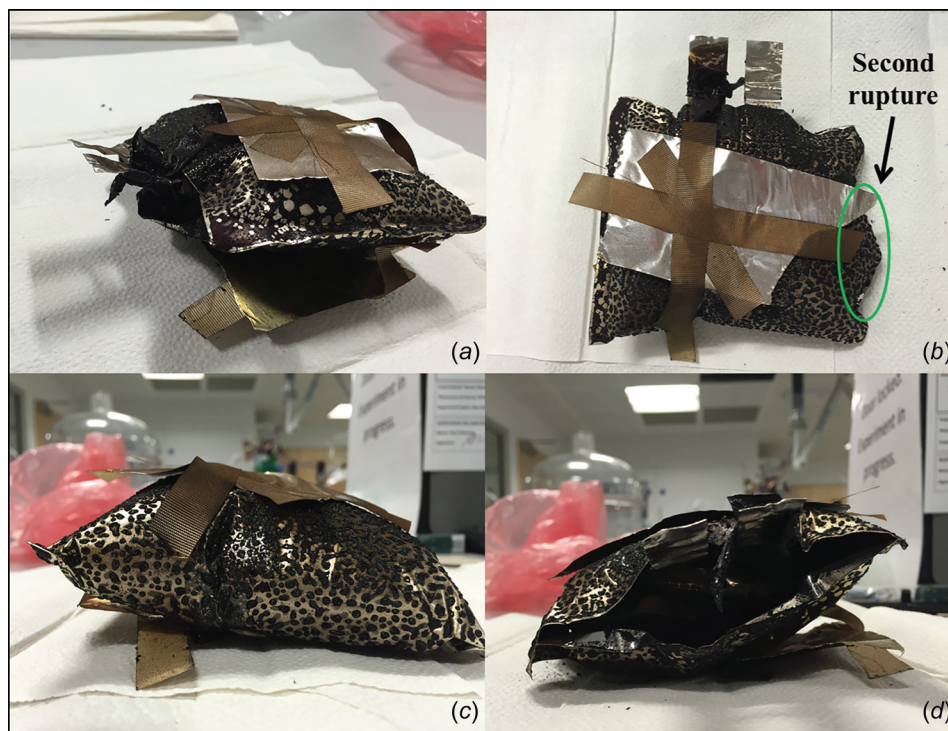
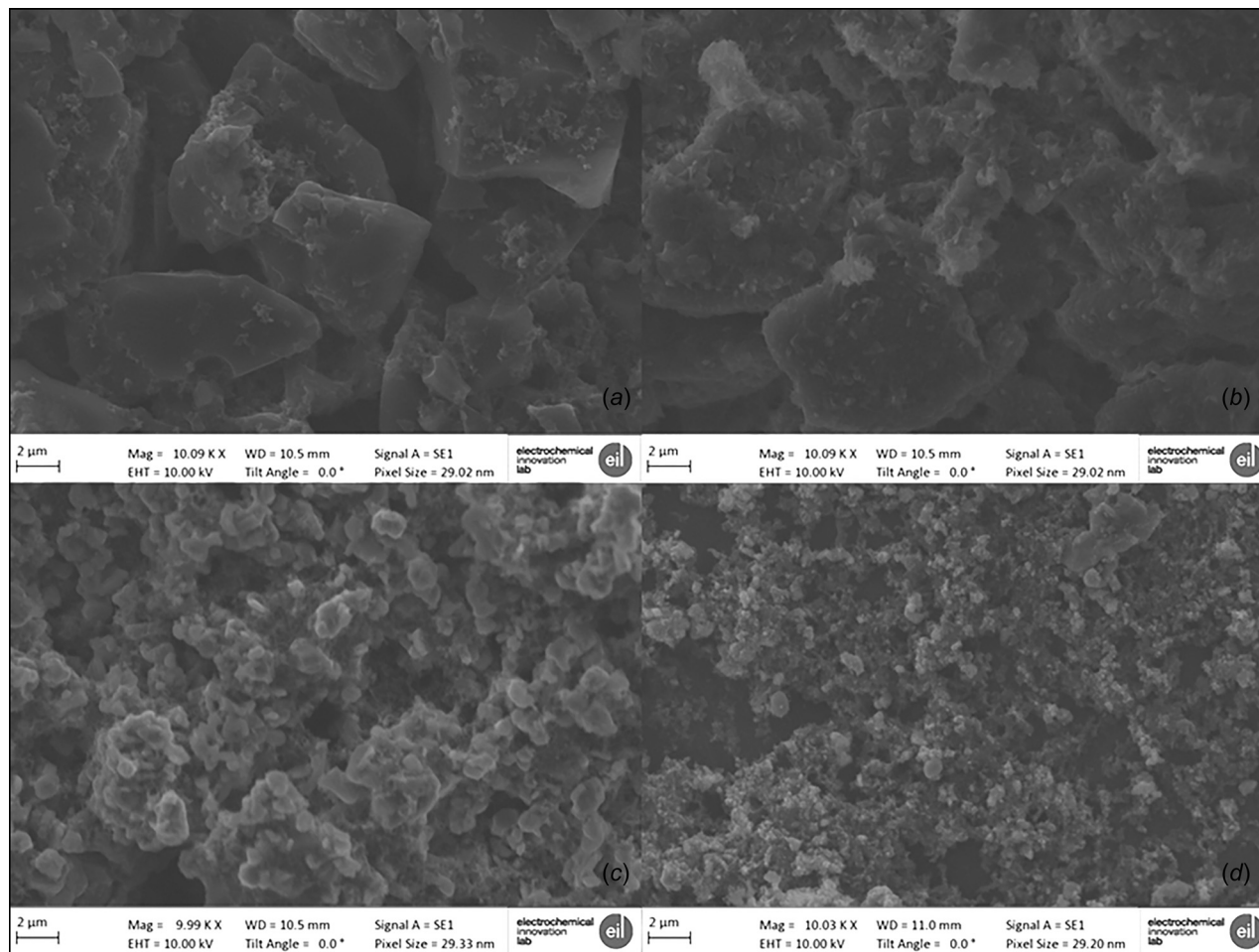


Fig. 6 NIB cell after ARC experiment-induced thermal runaway in the cell showing an (a) orthogonal view, (b) top view, (c) bottom view highlighting the swelling in the cell, and (d) top view showing the split which occurred in the pouch at the terminals



**Fig. 7** SEM images of (a) pristine, and (b) failed, negative electrodes from the LCO cell, (c) pristine  $\text{LiCoO}_2$  positive electrode, (d)  $\text{LiCoO}_2$  positive electrode after thermal runaway has occurred. All images are obtained using the SE1 signal at 15 kV accelerating voltage with magnifications of approximately 10,000 yielding a pixel size of 29 nm in all cases.

runaway has occurred; once more, this is likely due to gas generation at the cathode layer as a result of an interaction between the cathode and electrolyte. As with the NMM system, this gas generation has resulted in portions of the cathode being removed from the current collector with large areas of bare current collector visible in Fig. 8. The generation of gas due to thermal runaway has previously been reported by Golubkov et al. [31] who showed that the gases generated are typically a mix of alkanes, alkenes, and hydrogen, the ratios of which depend on the cathode chemistry employed. The SEM images shown in Fig. 7 suggest that thermal runaway reactions in NIB cells occur via a similar mechanism to that reported in Li-ion systems. Maleki et al. [40] suggested that thermal runaway in LCO/graphite systems (as used in this study) is initiated by the heat generated via the breakdown of the positive electrode and subsequent reaction with the electrolyte. The NIB cells in this study similarly show electrode degradation at the positive electrode, suggesting that it is also this layer which plays the largest part in the reactions which lead to thermal runaway.

## Conclusions

Accelerating rate calorimetry experiments comparing NIB containing a layered oxide positive electrode and commercial LIB containing  $\text{LiCoO}_2$  positive electrode have shown highlighted some important differences. NIB appears to have a shorter time to the first exothermic event that also occurs at a slightly lower temperature than LIB, while the rate of thermal runaway exhibited by Na-ion cells is lower than that observed in (LCO) cells. A shutdown separator present in the LCO cells significantly delays the

time taken to reach the onset of thermal runaway; however, it does not prevent thermal runaway in this case, which is comparable to the conditions experienced during a fire. This indicates that the solubility of the SEI layer in NIB is likely to be much greater than LIB, occurring in shorter time frames and at lower temperatures. However, the initial repeated dissolving and reforming of this SEI (as indicated by self-heating rates) observed in the battery, associated with elevated temperatures, is observed to be lower in NIB cells, suggesting this is a more stable cell both at temperatures below thermal runaway and during the thermal runaway process itself. The reduced degradation rate provided by the slower reaction kinetics may provide an opportunity to design a system to isolate or eject the cell in packs or modules.

Examination of the packs by X-ray CT shows significant distortions in the architecture of the cell packaging material in both instances. These are more significant in the NIB case which is ascribed to the sealing strategy of the cell. Such effects may be improved by optimization of the electrolyte, potentially using less volatile solvents. The distortions observed here are likely to induce mechanical stress within battery packs, which when coupled with the heating caused by a cell undergoing thermal runaway, may result in damage to and indeed the failure of neighboring cells, which must be addressed through adequate safety devices and quality control.

The internal architectures are destroyed in both cells, with the NIB showing a greater disparity from the original orientation of the layers. Despite this, the Al current collectors were seen to be largely intact on both electrodes in the NIB cell during post-mortem analysis, which indicates the temperature reached during thermal runaway could not have exceeded  $660^\circ\text{C}$ . In contrast, only

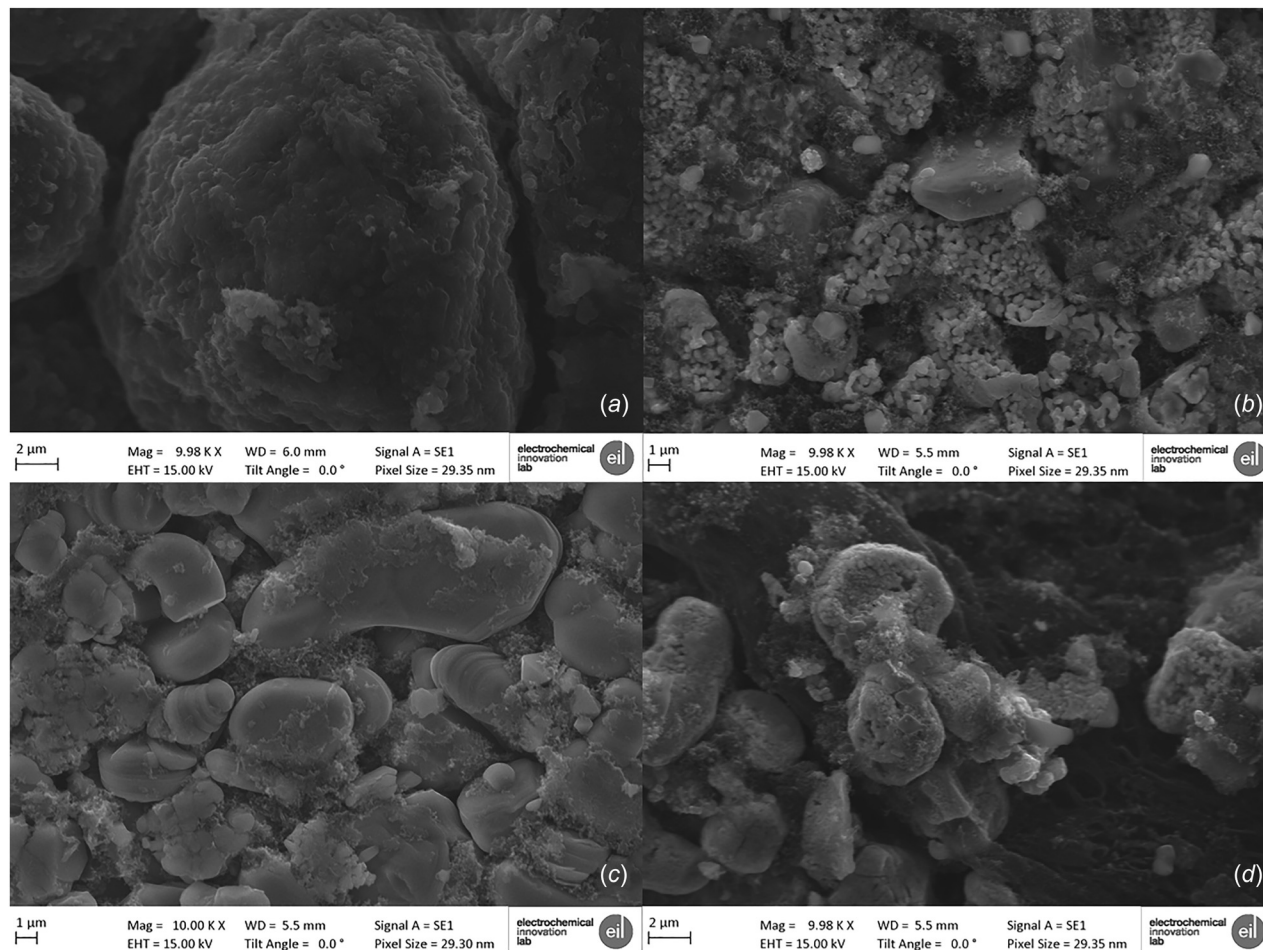


**Fig. 8 SEM images of (a) pristine, and (b) failed, negative electrodes from the LCO cell, (c) pristine LiCoO<sub>2</sub> positive electrode, (d) LiCoO<sub>2</sub> positive electrode after thermal runaway has occurred. All images are obtained using the SE1 signal at 15 kV accelerating voltage with magnifications of approximately 10,000 yielding a pixel size of 29 nm in all cases.**

the Cu current collector in the LCO cell remained intact; therefore, the maximum temperature reached during thermal runaway must be in the window  $660^{\circ}\text{C} < T_{\text{max}} < 1085^{\circ}\text{C}$ .

Scanning electron microscope shows significant changes in the microstructure of both the positive and negative electrodes of the LCO cell after thermal runaway; however, the negative electrode of the NIB cell retains a similar microstructure to that observed in a pristine cell anode. This suggests that the interaction between the positive electrode and the decomposed electrolyte is the major cause of thermal runaway, implying thermal runaway occurs in NIB cells via similar mechanisms to those reported for Li-ion systems.

### Acknowledgment

The authors would like to acknowledge the EPSRC funding for supporting the work of Robinson through the UCL Doctoral Fellowship scheme (EP/M507970/1) and the EPSRC for supporting the energy storage work in the Electrochemical Innovation Lab (EP/N032888/1; EP/N001583/1; EP/P009050/1; EP/M009394/1). The authors also acknowledge the STFC for supporting Shearing and Brett (ST/K00171X/1) and Royal Academy of Engineering for supporting Shearing, and Sharp Laboratories of Europe Ltd., for the NIB prototype cells.

### Funding Data

- Engineering and Physical Sciences Research Council (UCL Doctoral Prize).

### References

- [1] Armand, M., and Tarascon, J.-M., 2008, "Building Better Batteries," *Nature*, **451**(7179), pp. 652–657.
- [2] Lu, L., Han, X., Li, J., Hua, J., and Ouyang, M., 2013, "A Review on the Key Issues for Lithium-Ion Battery Management in Electric Vehicles," *J. Power Sources*, **226**, pp. 272–288.
- [3] Scrosati, B., Hassoun, J., and Sun, Y.-K., 2011, "Lithium-Ion Batteries. A Look Into the Future," *Energy Environ. Sci.*, **4**(9), pp. 3287–3295.
- [4] Beauregard, G. P., 2008, "Report of Investigation: Hybrids Plus Plug in Hybrid Electric Vehicle," U.S. Department of Energy, Idaho National Laboratory, Idaho Falls, ID, Report No. 5903.
- [5] JTSB, 2014, "Aircraft Serious Incident Investigation Report," All Nippon Airways Co., Ltd., Tokyo, Japan, Report No. JA804A.
- [6] AAIB, 2015, "Report on the Serious Incident to Boeing B787-8, ET-AOP London Heathrow Airport on 12 July 2013," Ethiopian Airlines, Addis Ababa, Ethiopia, Report No. EW/C2013/07/01.
- [7] NTSB, 2014, "Aircraft Incident Report, Auxiliary Power Unit Battery Fire, Japan Airlines Boeing 787-8, JA829J," National Transportation Safety Board, Washington, DC, Report No. NTSB/AIR-14/01.
- [8] Robinson, J. B., Darr, J. A., Eastwood, D. S., Hinds, G., Lee, P. D., Shearing, P. R., Taiwo, O. O., and Brett, D. J. L., 2014, "Non-Uniform Temperature Distribution in Li-Ion Batteries During Discharge—A Combined Thermal Imaging, X-ray Micro-Tomography and Electrochemical Impedance Approach," *J. Power Sources*, **252**, pp. 51–57.
- [9] Ellis, B. L., Makahnouk, W. R. M., Rowan-Weataluktuk, W. N., Ryan, D. H., and Nazar, L. F., 2010, "Crystal Structure and Electrochemical Properties of A<sub>2</sub>MPO<sub>4</sub>F Fluorophosphates (A = Na, Li; M = Fe, Mn, Co, Ni)," *Chem. Mater.*, **22**(3), pp. 1059–1070.
- [10] U.S. Geological Survey, 2008, "Mineral Commodity Summaries 2008," U.S. Geological Survey, Reston, VA.
- [11] Yang, Y., Hu, X., Qing, D., and Chen, F., 2013, "Arrhenius Equation-Based Cell-Health Assessment: Application to Thermal Energy Management Design of a HEV NiMH Battery Pack," *Energies*, **6**(5), p. 2709.
- [12] Khateeb, S. A., Farid, M. M., Selman, J. R., and Al-Hallaj, S., 2004, "Design and Simulation of a Lithium-Ion Battery With a Phase Change Material

- Thermal Management System for an Electric Scooter," *J. Power Sources*, **128**(2), pp. 292–307.
- [13] Galloway, R. C., and Haslam, S., 1999, "The ZEBRA Electric Vehicle Battery: Power and Energy Improvements," *J. Power Sources*, **80**(1–2), pp. 164–170.
- [14] Wang, J., Yang, J., Nuli, Y., and Holze, R., 2007, "Room Temperature Na/S Batteries With Sulfur Composite Cathode Materials," *Electrochem. Commun.*, **9**(1), pp. 31–34.
- [15] Arlt, T., Schroder, D., Krewer, U., and Manke, I., 2014, "In Operando Monitoring of the State of Charge and Species Distribution in Zinc Air Batteries Using X-ray Tomography and Model-Based Simulations," *Phys. Chem. Chem. Phys.*, **16**(40), pp. 22273–22280.
- [16] Lee, J.-S., Tai Kim, S., Cao, R., Choi, N.-S., Liu, M., Lee, K. T., and Cho, J., 2011, "Metal–Air Batteries With High Energy Density: Li–Air Versus Zn–Air," *Adv. Energy Mater.*, **1**(1), pp. 34–50.
- [17] Li, Y., and Dai, H., 2014, "Recent Advances in Zinc-Air Batteries," *Chem. Soc. Rev.*, **43**(15), pp. 5257–5275.
- [18] Palomares, V., Serras, P., Villaluenga, I., Hueso, K. B., Carretero-Gonzalez, J., and Rojo, T., 2012, "Na-Ion Batteries, Recent Advances and Present Challenges to Become Low Cost Energy Storage Systems," *Energy Environ. Sci.*, **5**(3), pp. 5884–5901.
- [19] Slater, M. D., Kim, D., Lee, E., and Johnson, C. S., 2013, "Sodium-Ion Batteries," *Adv. Funct. Mater.*, **23**(8), pp. 947–958.
- [20] Barker, J., and Wright, C. J., 2016, "Storage and/or Transportation of Sodium-Ion Cells," U. S. Patent No. [WO2016027082 A1](#).
- [21] Stevens, D. A., and Dahn, J. R., 2000, "High Capacity Anode Materials for Rechargeable Sodium-Ion Batteries," *J. Electrochem. Soc.*, **147**(4), pp. 1271–1273.
- [22] Kubota, K., and Komaba, S., 2015, "Review—Practical Issues and Future Perspective for Na-Ion Batteries," *J. Electrochem. Soc.*, **162**(14), pp. A2538–A2550.
- [23] Sun, Q., Ren, Q.-Q., Li, H., and Fu, Z.-W., 2011, "High Capacity  $\text{Sb}_2\text{O}_4$  Thin Film Electrodes for Rechargeable Sodium Battery," *Electrochem. Commun.*, **13**(12), pp. 1462–1464.
- [24] Xiao, L., Cao, Y., Xiao, J., Wang, W., Kovarik, L., Nie, Z., and Liu, J., 2012, "High Capacity, Reversible Alloying Reactions in SnSb/C Nanocomposites for Na-Ion Battery Applications," *Chem. Commun.*, **48**(27), pp. 3321–3323.
- [25] Jäckle, M., and Groß, A., 2014, "Microscopic Properties of Lithium, Sodium, and Magnesium Battery Anode Materials Related to Possible Dendrite Growth," *J. Chem. Phys.*, **141**(17), p. 174710.
- [26] Ellis, B. L., and Nazar, L. F., 2012, "Sodium and Sodium-Ion Energy Storage Batteries," *Curr. Opin. Solid State Mater. Sci.*, **16**(4), pp. 168–177.
- [27] Xiang, X., Zhang, K., and Chen, J., 2015, "Recent Advances and Prospects of Cathode Materials for Sodium-Ion Batteries," *Adv. Mater.*, **27**(36), pp. 5343–5364.
- [28] Vignarooban, K., Kushagra, R., Elango, A., Badami, P., Mellander, B. E., Xu, X., Tucker, T. G., Nam, C., and Kannan, A. M., 2016, "Current Trends and Future Challenges of Electrolytes for Sodium-Ion Batteries," *Int. J. Hydrogen Energy*, **41**(4), pp. 2829–2846.
- [29] Robinson, J. B., Engebretsen, E., Finegan, D. P., Darr, J., Hinds, G., Shearing, P. R., and Brett, D. J. L., 2015, "Detection of Internal Defects in Lithium-Ion Batteries Using Lock-In Thermography," *ECS Electrochem. Lett.*, **4**(9), pp. A106–A109.
- [30] Bandhauer, T. M., Garimella, S., and Fuller, T. F., 2011, "A Critical Review of Thermal Issues in Lithium-Ion Batteries," *J. Electrochem. Soc.*, **158**(3), pp. R1–R25.
- [31] Golubkov, A. W., Fuchs, D., Wagner, J., Wiltche, H., Stangl, C., Fauler, G., Voitic, G., Thaler, A., and Hacker, V., 2014, "Thermal-Runaway Experiments on Consumer Li-Ion Batteries With Metal-Oxide and Olivin-Type Cathodes," *RSC Adv.*, **4**(7), pp. 3633–3642.
- [32] Eastwood, D. S., Yufit, V., Gelb, J., Gu, A., Bradley, R. S., Harris, S. J., Brett, D. J. L., Brandon, N. P., Lee, P. D., Withers, P. J., and Shearing, P. R., 2014, "Lithiation-Induced Dilation Mapping in a Lithium-Ion Battery Electrode by 3D X-Ray Microscopy and Digital Volume Correlation," *Adv. Energy Mater.*, **4**(4), p. 1300506.
- [33] Vetter, J., Novák, P., Wagner, M. R., Veit, C., Möller, K. C., Besenhard, J. O., Winter, M., Wohlfahrt-Mehrens, M., Vogler, C., and Hammouche, A., 2005, "Ageing Mechanisms in Lithium-Ion Batteries," *J. Power Sources*, **147**(1–2), pp. 269–281.
- [34] Broussely, M., Biensan, P., Bonhomme, F., Blanchard, P., Herreyre, S., Nechev, K., and Staniewicz, R. J., 2005, "Main Aging Mechanisms in Li Ion Batteries," *J. Power Sources*, **146**(1–2), pp. 90–96.
- [35] Finegan, D. P., Scheel, M., Robinson, J. B., Tjaden, B., Di Michiel, M., Hinds, G., Brett, D. J. L., and Shearing, P. R., 2016, "Investigating Lithium-Ion Battery Materials During Overcharge-Induced Thermal Runaway: An Operando and Multi-Scale X-Ray CT Study," *Phys. Chem. Chem. Phys.*, **8**(45), pp. 30912–30919.
- [36] Finegan, D. P., Scheel, M., Robinson, J. B., Tjaden, B., Hunt, I., Mason, T. J., Millichamp, J., Di Michiel, M., Offer, G. J., Hinds, G., Brett, D. J. L., and Shearing, P. R., 2015, "In-Operando High-Speed Tomography of Lithium-Ion Batteries During Thermal Runaway," *Nat. Commun.*, **6**, p. 6924.
- [37] Finegan, D. P., Tudisco, E., Scheel, M., Robinson, J. B., Taiwo, O. O., Eastwood, D. S., Lee, P. D., Di Michiel, M., Bay, B., Hall, S. A., Hinds, G., Brett, D. J. L., and Shearing, P. R., 2015, "Quantifying Bulk Electrode Strain and Material Displacement Within Lithium Batteries Via High-Speed Operando Tomography and Digital Volume Correlation," *Adv. Sci.*, **3**(3), p. 1500332.
- [38] Xia, X., and Dahn, J. R., 2012, "NaCrO<sub>2</sub> is a Fundamentally Safe Positive Electrode Material for Sodium-Ion Batteries With Liquid Electrolytes," *Electrochem. Solid-State Lett.*, **15**(1), pp. A1–A4.
- [39] von Sacken, U., Nodwell, E., Sundher, A., and Dahn, J. R., 1995, "Comparative Thermal Stability of Carbon Intercalation Anodes and Lithium Metal Anodes for Rechargeable Lithium Batteries," *J. Power Sources*, **54**(2), pp. 240–245.
- [40] Maleki, H., Deng, G., Anani, A., and Howard, J., 1999, "Thermal Stability Studies of Li-Ion Cells and Components," *J. Electrochem. Soc.*, **146**(9), pp. 3224–3229.
- [41] Richard, M. N., and Dahn, J. R., 1999, "Accelerating Rate Calorimetry Study on the Thermal Stability of Lithium Intercalated Graphite in Electrolyte—II: Modeling the Results and Predicting Differential Scanning Calorimeter Curves," *J. Electrochem. Soc.*, **146**(6), pp. 2078–2084.
- [42] Smith, K., Treacher, J., Ledwoch, D., Adamson, P., and Kendrick, E., 2017, "Novel High Energy Density Sodium Layered Oxide Cathode Materials: From Material to Cells," *ECS Trans.*, **75**(22), pp. 13–24.
- [43] Chen, Z., Qin, Y., Ren, Y., Lu, W., Orendorff, C., Roth, E. P., and Amine, K., 2011, "Multi-Scale Study of Thermal Stability of Lithiated Graphite," *Energy Environ. Sci.*, **4**(10), pp. 4023–4030.
- [44] Orendorff, C. J., 2012, "The Role of Separators in Lithium-Ion Cell Safety," *Electrochem. Soc. Interface*, **21**(2), pp. 61–65.
- [45] Finegan, D. P., Cooper, S. J., Tjaden, B., Taiwo, O. O., Gelb, J., Hinds, G., Brett, D. J. L., and Shearing, P. R., 2016, "Characterising the Structural Properties of Polymer Separators for Lithium-Ion Batteries in 3D Using Phase Contrast X-ray Microscopy," *J. Power Sources*, **333**, pp. 184–192.
- [46] Irisarri, E., Ponrouch, A., and Palacin, M. R., 2015, "Review—Hard Carbon Negative Electrode Materials for Sodium-Ion Batteries," *J. Electrochem. Soc.*, **162**(14), pp. A2476–A2482.
- [47] Guo, W.-M., Xiao, H.-N., and Zhang, G.-J., 2008, "Kinetics and Mechanisms of Non-Isenthalpic Oxidation of Graphite in Air," *Corros. Sci.*, **50**(7), pp. 2007–2011.
- [48] McKee, D. W., 1970, "Metal Oxides as Catalysts for the Oxidation of Graphite," *Carbon*, **8**(5), pp. 623–635.